

ChemComm

Accepted Manuscript



This is an *Accepted Manuscript*, which has been through the Royal Society of Chemistry peer review process and has been accepted for publication.

Accepted Manuscripts are published online shortly after acceptance, before technical editing, formatting and proof reading. Using this free service, authors can make their results available to the community, in citable form, before we publish the edited article. We will replace this *Accepted Manuscript* with the edited and formatted *Advance Article* as soon as it is available.

You can find more information about *Accepted Manuscripts* in the [Information for Authors](#).

Please note that technical editing may introduce minor changes to the text and/or graphics, which may alter content. The journal's standard [Terms & Conditions](#) and the [Ethical guidelines](#) still apply. In no event shall the Royal Society of Chemistry be held responsible for any errors or omissions in this *Accepted Manuscript* or any consequences arising from the use of any information it contains.

COMMUNICATION

Mapping functional groups on oxidised multi-walled carbon nanotubes at the nanometre scale

Cite this: DOI: 10.1039/x0xx00000x

A. E. Goode,^a N. D. M. Hine,^b S. Chen,^a S. D. Bergin,^c M. S. P. Shaffer,^d M. P. Ryan,^a P. D. Haynes,^{a,e} A. E. Porter^a and D. W. McComb^fReceived 00th January 2012,
Accepted 00th January 2012

DOI: 10.1039/x0xx00000x

www.rsc.org/

Despite voluminous research on the acid oxidation of carbon nanotubes (CNTs), there is a distinct lack of experimental results showing distributions of functional groups at the nanometre length scale. Here, functional peaks have been mapped across individual multi-walled CNTs with low-dose, monochromated electron energy-loss spectroscopy (EELS) in the scanning transmission electron microscope (STEM). Density functional theory simulations show EELS features are consistent with oxygenated functional groups, most likely carboxyl moieties.

Acid-oxidation is used extensively in the processing of carbon nanotubes (CNTs), to improve both the purity and the solubility of CNT samples. Treatment with acids, typically nitric and sulphuric,^{1,2} increases sample purity by removing metallic catalyst and carbonaceous debris³. Acid oxidation is known to open the ends of CNTs⁴, cause controllable length shortening⁵, and introduce structural defects such as atomic vacancies and deviations from hexagonal ring structures⁶. Additionally, oxidised CNTs (ox-CNTs) are often further derivatised, introducing additional functional groups for wide-ranging applications⁷.

A thorough understanding of the effects of acid oxidation, *i.e.* altered surface and physicochemical properties, is important both for their applications and the ability to control the oxidation and subsequent functionalisation processes. Changes to CNT dimensions and defect density following acid oxidation have been well characterised using imaging techniques such as high resolution transmission electron microscopy (HRTEM) and scanning electron microscopy (SEM)^{8,9}. To study the chemistry of ox-CNTs, a range of techniques are commonly employed, namely infrared spectroscopy, Raman spectroscopy, chemical derivatisation, thermogravimetric analysis, Boehm titration, temperature programmed desorption, x-ray photoelectron spectroscopy and x-ray absorption spectroscopy (XAS)¹⁰. While these techniques provide information on the identity and number of functional groups present in bulk samples of ox-CNTs, they provide only limited *spatially-resolved* information.

As many functional groups are charged, their spatial distribution will have a large influence on the electrostatic interactions between two CNTs as well as between a CNT and its environment, *e.g.* interactions between CNTs and polymers in composites, or between CNTs and biomolecules or membranes in the field of nanomedicine. Knowledge of the *distribution* of functional groups across individual CNTs would facilitate better understanding of the mechanisms of oxidation, and could subsequently lead to increased control over the oxidation process. Functionalisation is expected at the sites of highest chemical reactivity on a CNT: at the ends, and at defects in the sidewalls⁷. Indeed, Ag nanoparticle tags have demonstrated the presence of functional groups at both CNT ends¹¹ and sidewalls¹², however such tagging methods are indirect and seldom quantitative. Very few techniques are available to directly probe spatially-resolved chemical information at the nanometre scale. Recently, Hitchcock *et al.*¹³ demonstrated the capability of XAS in the scanning transmission x-ray microscope (STXM) for mapping oxidised multi-walled carbon nanotubes (ox-MWNTs). Currently, the smallest reported probe size¹⁴ in an STXM is ~10 nm, too large for individual single-walled nanotubes (SWNTs), and much larger than the size of many functional groups. Therefore there is a need for methods capable of characterising ox-CNTs at a finer length scale. Electron energy-loss spectroscopy (EELS) in the scanning transmission electron microscope (STEM) can provide chemical information analogous to XAS, but with sub-nanometre spatial resolutions. However, due to electron beam induced damage, EELS has often been considered unsuitable for study of the fine structure at the carbon K-edge^{15,16}. This communication demonstrates that low-dose EELS is in fact capable of detecting changes in electronic structure characteristic of ox-MWNTs, and that these changes can be mapped across individual nanotubes. Density functional theory (DFT) simulations suggest that the EELS fine structure observed in ox-MWNTs originates from carbon atoms associated with a C=O bond, likely carboxyl adgroups.

Commercial MWNTs were purchased from Arkema SA (Lacq-Mourenx, France). As-received, pristine MWNTs (p-MWNTs) were acid-oxidised following a standard procedure (reflux in concentrated HNO₂/H₂SO₄). The ox-MWNTs were base-washed to remove

carbonaceous debris¹⁷. Raman measurements using an excitation of 632.8 nm found G:D peak ratios of 0.88 ± 0.02 for p-MWNTs and 0.75 ± 0.05 for ox-MWNTs, indicating a degree of damage to the graphitic network, as expected.

For EELS experiments, lacey carbon TEM grids were prepared by heating overnight at 120 °C under vacuum to reduce carbon contamination. MWNT samples were tip-sonicated in HPLC-grade water for 2-3 minutes, before being drop cast onto TEM grids. Monochromated STEM-EELS was performed in an FEI Titan microscope, with an accelerating voltage of 80 kV, energy resolution of 0.2 eV and convergence and collection semi-angles of 7 and 18 mrad respectively. The experiment was designed to minimise the electron dose (electrons per Å²); spectrum images were acquired using relatively large pixel sizes of 3-15 nm, and with sub-pixel scanning enabled. All EELS maps presented here were acquired with pixel sizes of $\sim 5 \text{ nm} \times 5 \text{ nm}$, at the carbon K-edge. O K-edge data (Figure S1) confirm the presence of oxygen in the system but the signal to noise ratio is too low for detailed mapping. The majority of data were recorded with a dose of 10^5 electrons/Å² or less. This is consistent with doses used in the literature by other authors¹⁸, and HRTEM imaging (figure S4) shows that these doses have little effect on CNT graphitic structure. As the predominant damage mechanism at 80 kV is expected to be radiolytic damage, samples were cooled to -70°C in a Gatan liquid nitrogen cold stage to mitigate diffusion processes. Spectra were processed by removing background of the form $Ae^{-\lambda}$, and aligning the $1s-\pi^*$ peak maximum to 285.5 eV.

Figure 1a displays EEL spectra obtained from a pristine (black) and oxidised (orange) MWNT. Both spectra contain peaks A and C, at 285.5 eV and 292.7 eV respectively, which originate from the $1s-\pi^*$ and $1s-\sigma^*$ transitions of graphitic carbon. These features are in good agreement with previously reported XAS and EEL spectra of CNTs¹⁹⁻²². Some EEL spectra from ox-MWNTs exhibit an additional peak B, at 287.7 eV. This peak was mostly observed as a relatively weak feature; however, a number of spectra exhibited a sharp, intense peak B. In a few instances, weak features at 287.7 eV were also observed in p-MWNT spectra.

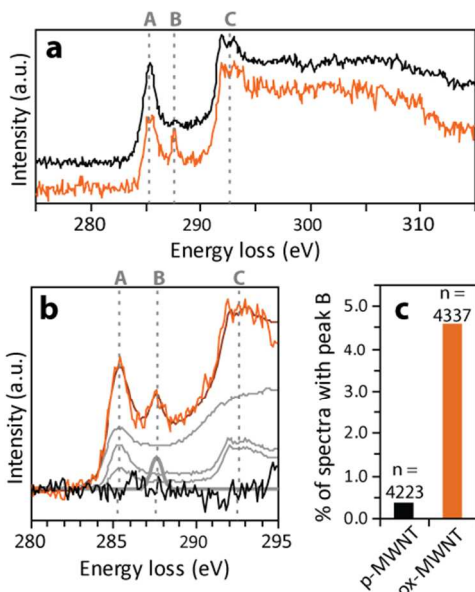


Figure 1. (a) EEL spectra from pristine (black) and oxidised (orange) MWNTs. Peak B at 287.7 eV is present in spectra from ox-MWNTs. (b) Example of an ox-MWNT spectrum (orange) decomposed into four components (gray) with fitted spectrum (brown) and residual signal (black). (c) Bar graph showing percentage of spectra containing a statistically significant peak B. The total number of spectra analysed, n , is given; in both cases this corresponds to ~ 50 CNTs.

To perform more detailed analysis of the datasets, each EEL spectrum was decomposed using singular value decomposition (SVD). Four components were used for spectrum fitting: (i) a Gaussian peak centred at 287.7 eV, (ii) graphitic carbon in the orientation where the momentum transfer \mathbf{q} is parallel to the c axis of the CNT¹⁹, (iii) graphitic carbon with \mathbf{q} perpendicular to c axis and (iv) amorphous carbon from the support film, defects and carbonaceous debris. Two components (ii and iii) were required to fully describe the orientation-dependence of the graphitic signal from the CNTs (Figure S2). Figure 1b shows an example of a fitted ox-MWNT EEL spectrum. The black line shows the residual signal, *i.e.* the difference between experimental and fitted spectra.

EEL spectra contained low signal-to-noise ratios (SNR) due to the short spectrum acquisition times used to minimise the electron dose. To distinguish between weak features and noise, statistical analysis was performed on all datasets. This analysis compared the height (H) of the fitted gaussian peak to the spectral noise, approximated as the residual signal after SVD fitting. The standard deviation of this 'noise', σ , was calculated between 286-290 eV where EEL spectra of p-MWNTs are relatively flat. Peak B was determined to be statistically significant if

$$H > 2.33 \times \sigma_{286-290}$$

The choice of 2.33σ corresponds to a probability of 99% that the height of peak B cannot be explained by spectral noise²³. Figure 1c displays the percentage of EEL spectra which contain statistically significant peaks B at 287.7 eV. Feature B was observed approximately ten times more frequently in the ox-MWNT sample compared to p-MWNTs. However, the incidence of observing peak B in ox-MWNT spectra was still low, at $\sim 5\%$.

Chemical maps for the components used in SVD fitting were calculated for each spectrum image. Figure 2 shows maps from a selected MWNT, as well as a HRTEM image of the same MWNT recorded after EELS analysis. The SVD components (ii) and (iii) have been combined into a single map of graphitic carbon, showing that the graphitic structure has been preserved along the entire length of the ox-MWNTs. Peak B at 287.7 eV appears to be inhomogeneously distributed across the ox-MWNTs, with the highest concentration located in box 1, where a number of the outer walls of the MWNT appear to have open ends. There is no evidence of higher concentrations of peak B at the bend in the MWNT (figures 2a and S3), contrary to the commonly quoted prediction of higher functional group loading at the kinks of MWNTs^{24, 25}. However, it is possible that functional groups are present in such locations, below the detection limit of these measurements.

The EELS fine structure between peaks A and C reported here is distinct from previous XAS studies^{5, 21, 26, 27} of oxidised graphitic materials. Interestingly, the dominant feature in most XAS data occurs at a higher energy-loss, around 288.5 eV. This feature, which is not observed in any EEL spectra, is often assigned to carboxyl groups²¹. However, as Zhong *et al.* describe¹¹, peaks at 288.5 eV may be caused by carbonaceous contamination which originates from the carbon support films; similar contamination has been reported in the STEM²⁸. In this work, pre-treatment of the TEM grids prevents the formation of a carbonaceous coating on MWNTs (Figure S4). A number of XAS studies also report secondary features at ~ 287.7 eV, attributing this intensity to "oxygen-containing surface functional groups"^{21, 26} or (unspecified) defects in the graphitic structure²⁷, though there is no consensus on the specific moiety giving rise to this peak.

To examine the feasibility of various possible candidate structures for peak B, EEL spectra were simulated using plane-wave DFT calculations as implemented in the CASTEP code^{29, 30}. A pristine (16,0) CNT was constructed in a 256-atom supercell comprising four

copies of the primitive unit cell along the tube axis for a 17.1 Å repeat length, with a 20×20 Å box perpendicular to the tube axis. Ultrasoft pseudopotentials were used for all species, and the local density approximation (LDA) for exchange and correlation was used. A plane-wave cut-off energy of 500 eV and 22 k-points along the tube axis were found to be sufficient for convergence of the EELS calculations. We simulate the EEL spectra originating from the C 1s core level, in the dipole approximation, individually for each atom. Core-hole effects are included by promoting half an electron from 1s to 2p during pseudopotential generation for the chosen atom, as this has been found to be reliable for carbon nanomaterials in previous work³¹. A Lorentzian broadening of 0.2 eV was applied to the calculated EEL spectra to approximate the experimental resolution.

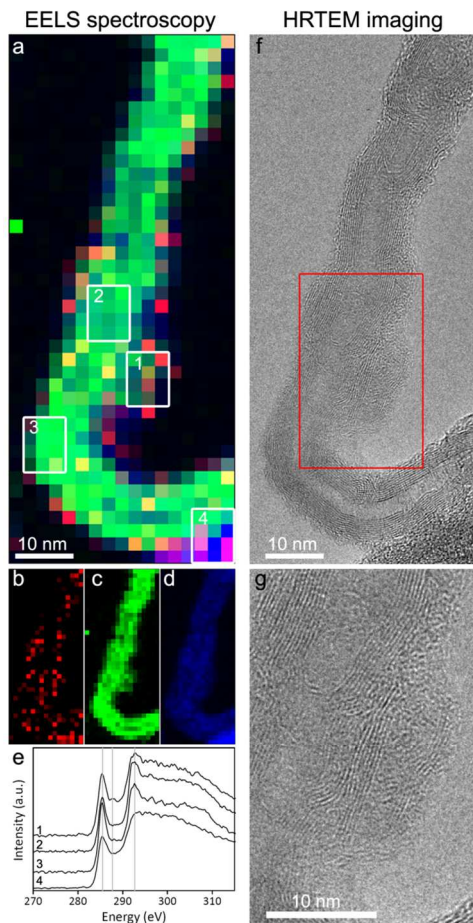


Figure 2. (a) Chemical map calculated by SVD fitting of EELS results. Red, green and blue regions contain contributions from peak B, graphitic carbon, and amorphous carbon, respectively. (b-d) Individual maps of the fitting components from (a). (e) EEL spectra from boxed regions in (a). (f) HRTEM image of the same ox-MWNT, after EELS data has been acquired, and (g) higher magnification image of boxed region in (f).

Dotted lines in each subfigure of Figure 3b show calculated spectra for the pristine (16,0) SWNT: the same spectral features are seen as in Figure 1 for the p-MWNT samples. In particular, peaks A and C, originating from 1s- π^* and 1s- σ^* transitions, are seen clearly, exhibiting similar widths and separations as in Figure 1. The energy scale in all figures is aligned so that the 1s- π^* peak lies at 285.5 eV. The pristine tube shows some weak structuring between the A and C peaks, but this is strongly dependent on the chosen tube radius, and is an artefact of the relatively small size of the simulated nanotube. These weak structures are not expected to be observed in larger or multi-walled nanotubes.

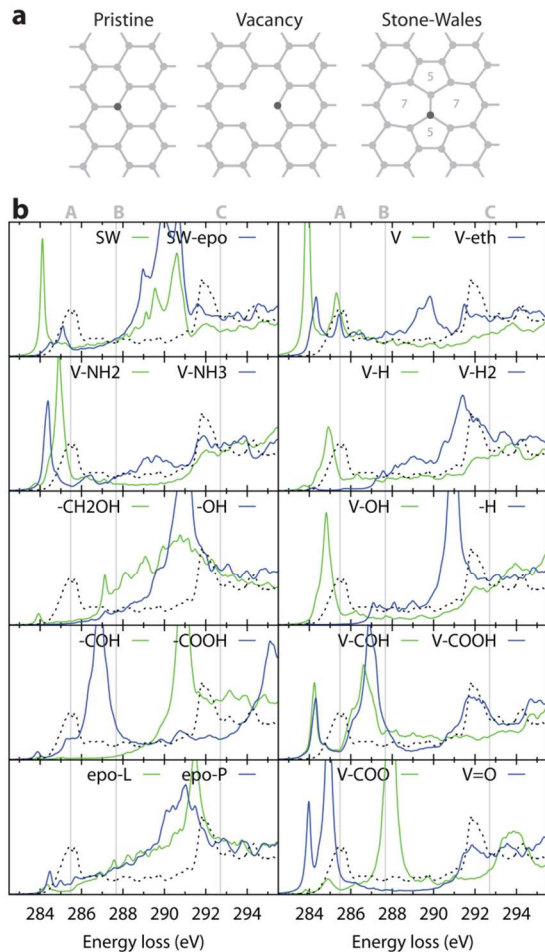


Figure 3. Simulated structures and EEL spectra from plane-wave DFT calculations. (a) Idealized schematic of unrelaxed defect structures in the graphitic network of the CNT walls, onto which functional adgroups are attached, out of plane. For relaxed structures see Figure S5. Adgroups attach to the carbon atom shaded black. (b) Simulated EEL spectra for C atoms in defect structures are plotted in green and blue. Spectra for the pristine nanotube are overlaid (dotted line).

A selection of feasible defect structures was created, and relaxed coordinates were calculated using geometry relaxation (with a criterion for the maximum force of 0.05 eV/Å on any atom). The defects simulated consisted of: vacancy (V-); vacancy with carbonyl group (V=O); vacancy with hydroxyl group (V-OH); vacancy with ether adjacent to V site (V-eth); adatom oxygen in an epoxy configuration, either on a bond parallel to the tube axis (epo-L) or at 60° (epo-P); Stone-Wales defect (SW), and SW defect with epoxy oxygen on the C-C bond between two heptagons (SW-epo); aldehyde sidewall adgroup (-COH); carboxyl sidewall adgroup (-COOH); methanol sidewall adgroup (-CH₂OH); hydroxyl sidewall adgroup (-OH); vacancy with aldehyde adgroup (V-COH); vacancy with carboxyl adgroup (V-COOH); vacancy with carboxylate group (V-COO); vacancy with H and 2H (V-H, V-2H); sidewall -H; vacancy with NH₂ and NH₃ adgroups (V-NH₂, V-NH₃). Relaxed structures are shown in the supporting information (Figure S5). Simulated EEL spectra of chosen carbon atoms in each structure are shown in Figure 3. The chosen carbon atoms are shown as darker balls in Figure S5. High-curvature fullerene-like defects were also considered (Figure S6-8) but did not display features at 287.7 eV.

Firstly, spectra of V, V-H, V-2H and SW configurations show that straightforward damage to the CNT consisting of knocking out individual atoms to leave dangling bonds or -H terminations does

not produce strong peaks that could explain peak B. In most cases the sp^2 -network is not significantly affected and thus no major peak shifts are observed. Likewise, V-NH₂ and V-NH₃ do not produce suitable candidate peaks.

Next, all oxygen-containing configurations tend to produce very strongly affected spectra, due to the strong influence of the oxygen atom on the carbon. Configurations containing C=O produce sharp peaks due to the localised states induced by the double bond. In particular, as the electron-withdrawing power of the defect increases, e.g. from V=O to V-COOH to V-COO, a strong peak is observed at increasing offset from the sp^2 peak A. Epoxide configurations which disrupt the sp^2 network and produce local sp^3 bonding appear to create broader peaks at higher energies above 290 eV.

The narrow linewidth and consistent offset of peak B from peak A in the experimental spectra thus suggests that the peak B originates from C atoms associated with a specific oxygen defect containing a C=O bond. As seen in the spectrum for -COOH and -V-COO, such carboxyl and carboxylate groups appear a likely candidate on the basis of the position of the candidate for peak B relative to peak A in the same system. It is not possible to determine what precise geometry the carboxyl might be in from the simulation results, as the spectra for V-COOH, -COOH and presumably a range of other COOH-containing groups all have a peak at a similar offset from the $1s-\pi^*$ peak A.

Conclusions

To conclude, using 80 kV STEM-EELS at -70°C, peak B at 287.7 eV was observed in spectra of MWNT oxidised using H₂SO₄/HNO₃. This peak was less prevalent in MWNT samples prior to acid oxidation. We hypothesise that this feature arises from oxygen-containing functional groups on the MWNT surface. DFT calculations suggest an assignment to carboxyl or carboxylate-containing defect species, with -COOH or -COO groups being the closest matched of those tested. Thus, peak B has been used as a signature of the oxidation process. Quantifying the number of groups present, while highly desirable, would be non-trivial due to the strong orientation dependence of this signal and requirement for high SNR. Peak B has been mapped across individual MWNTs with a spatial resolution of ~5 nm, showing that these groups are inhomogeneously distributed across the entire length of the MWNTs. The capability of STEM-EELS and DFT in mapping and understanding new spectral features associated with functional groups on ox-MWNT samples has been demonstrated. More generally, these analytical results open the door for compelling new sets of EELS experiments that can provide detailed information about the distribution and chemical nature of functional groups on the surface of carbon, and other, nanoparticle systems.

Funding was provided by EPSRC Science and Innovation Programme: EP/D063329, ERC starting investigator grant #257182 (AP), and the Royal Society (PDH). NDMH acknowledges the support of EPSRC grant EP/J015059/1, a Leverhulme ECF, and the Winton Programme for the Physics of Sustainability.

Notes and references

^a Department of Materials, Imperial College London, London, UK.

^b Cavendish Laboratory, J. J. Thomson Avenue, Cambridge, UK.

^c School of Physics and CRANN, Trinity College, Dublin 2, Ireland.

^d Department of Chemistry, Imperial College London, London, UK.

^e Department of Chemistry, Imperial College London, London, UK.

^f Department of Materials Science and Engineering, The Ohio State University, Ohio 43210, USA.

Electronic Supplementary Information (ESI) available: [Methods, O K-edge data, SVD fitting results, HRTEM images and relaxed defect structures]. See DOI: 10.1039/c000000x/

1. K. Hernadi, A. Siska, L. Thien-Nga, L. Forro and I. Kiricsi, *Solid State Ionics*, 2001, **141**, 203-209.
2. J. Zhang, H. L. Zou, Q. Qing, Y. L. Yang, Q. W. Li, Z. F. Liu, X. Y. Guo and Z. L. Du, *J. Phys. Chem. B*, 2003, **107**, 3712-3718.
3. A. G. Rinzler, J. Liu, H. Dai, P. Nikolaev, C. B. Huffman, F. J. Rodriguez-Macias, P. J. Boul, A. H. Lu, D. Heymann, D. T. Colbert, R. S. Lee, J. E. Fischer, A. M. Rao, P. C. Eklund and R. E. Smalley, *Applied Physics a-Materials Science & Processing*, 1998, **67**, 29-37.
4. M. S. P. Shaffer, X. Fan and A. H. Windle, *Carbon*, 1998, **36**, 1603-1612.
5. J. Cho, A. R. Boccaccini and M. S. P. Shaffer, *Carbon*, 2012, **50**, 3967-3976.
6. T. Saito, K. Matsushige and K. Tanaka, *Physica B*, 2002, **323**, 280-283.
7. N. Karousis, N. Tagmatarchis and D. Tasis, *Chemical Reviews*, 2010, **110**, 5366-5397.
8. G. A. Forrest and A. J. Alexander, *J. Phys. Chem. C*, 2007, **111**, 10792-10798.
9. C. A. Furtado, U. J. Kim, H. R. Gutierrez, L. Pan, E. C. Dickey and P. C. Eklund, *J. Am. Chem. Soc.*, 2004, **126**, 6095-6105.
10. K. A. Wepasnick, B. A. Smith, J. L. Bitter and D. H. Fairbrother, *Analytical and Bioanalytical Chemistry*, 2010, **396**, 1003-1014.
11. J. Liu, A. G. Rinzler, H. J. Dai, J. H. Hafner, R. K. Bradley, P. J. Boul, A. Lu, T. Iverson, K. Shelimov, C. B. Huffman, F. Rodriguez-Macias, Y. S. Shon, T. R. Lee, D. T. Colbert and R. E. Smalley, *Science*, 1998, **280**, 1253-1256.
12. R. Menzel, M. Q. Tran, A. Menner, C. W. M. Kay, A. Bismarck and M. S. P. Shaffer, *Chemical Science*, 2010, **1**, 603-608.
13. A. P. Hitchcock, E. Najafi, M. Obst, J.-J. Pireaux, B. Douhard and A. Felten, *Microsc Microanal*, 2008, **14**.
14. W. Chao, P. Fischer, T. Tyliczszak, S. Rekawa, E. Anderson and P. Naulleau, *Opt Express*, 2012, **20**.
15. A. Braun, A. Kubatova, S. Wirick and S. B. Mun, *J. Electron Spectrosc. Relat. Phenom.*, 2009, **170**, 42-48.
16. D. Alexander, J. Anderson, L. Forró and P. Crozier, *Microscopy and Microanalysis*, 14 (Suppl. 2), 2008, 674-675.
17. R. Verdejo, S. Lamoriniere, B. Cottam, A. Bismarck and M. Shaffer, *Chemical Communications*, 2007, 513-515.
18. A. L. Koh, E. Gidcumb, O. Zhou and R. Sinclair, *Acs Nano*, 2013, **7**, 2566-2572.
19. O. Stephan, M. Kociak, L. Henrard, K. Suenaga, A. Gloter, M. Tence, E. Sandre and C. Colliex, *J. Electron Spectrosc. Relat. Phenom.*, 2001, **114**, 209-217.
20. A. P. Hitchcock, E. Najafi, J. A. Wang, J. W. Guan, S. Denomme and B. Simard, *J. Am. Chem. Soc.*, 2010, **132**, 9020-9029.
21. A. Kuznetsova, I. Popova, J. T. Yates, M. J. Bronikowski, C. B. Huffman, J. Liu, R. E. Smalley, H. H. Hwu and J. G. G. Chen, *J. Am. Chem. Soc.*, 2001, **123**, 10699-10704.
22. M. Abbas, Z. Y. Wu, J. Zhong, K. Ibrahim, A. Fiori, S. Orlanducci, V. Sessa, M. L. Terranova and I. Davoli, *Applied Physics Letters*, 2005, **87**.
23. P. C. Meier and R. E. Zund, *Statistical Methods in Analytical Chemistry*, Second Edition edn., John Wiley & Sons, Inc., 2000.
24. S. C. Tsang, P. J. F. Harris and M. L. H. Green, *Nature*, 1993, **362**, 520-522.
25. D. Srivastava, D. W. Brenner, J. D. Schall, K. D. Ausman, M. F. Yu and R. S. Ruoff, *J. Phys. Chem. B*, 1999, **103**, 4330-4337.
26. E. Najafi, J. A. Wang, A. P. Hitchcock, J. W. Guan, S. Denomme and B. Simard, *J. Am. Chem. Soc.*, 2010, **132**, 9020-9029.
27. V. A. Coleman, R. Knut, O. Karis, H. Grennberg, U. Jansson, R. Quinlan, B. C. Holloway, B. Sanyal and O. Eriksson, *J. Phys. D-Applied Physics*, 2008, **41**.
28. C. M. McGilvery, A. E. Goode, M. S. P. Shaffer and D. W. McComb, *Micron*, 2012, **43**, 450-455.
29. S. J. Clark, M. D. Segall, C. J. Pickard, P. J. Hasnip, M. J. Probert, K. Refson and M. C. Payne, *Z. Kristallogr*, 2005, **220**, 567-570.
30. S. P. Gao, C. J. Pickard, A. Perlov and V. Milman, *J. Phys.-Condensed Matter*, 2009, **21**.
31. K. Suenaga and M. Koshino, *Nature*, 2010, **468**, 1088-1090.